Anchoring Co_3O_4 on CdZnS to accelerate hole migration for highly stable photocatalytic overall water splitting

Kai Yu [a], Tianyang Zhang [a], Yingming Wang [a], Jie Wu [a], Hui Huang [a], Kui Yin [a,*], Fan Liao [a,*], Yang Liu [a,*], Zhenhui Kang [a,b]

[a] Institute of Functional Nano & Soft Materials (FUNSOM), Jiangsu Key Laboratory for Carbon-Based Functional Materials & Devices, Soochow University, 199 Ren'ai Road, Suzhou 215123, Jiangsu, China
[b] Macao Institute of Materials Science and Engineering (MIMSE), MUST-SUDA Joint Research Center for Advanced Functional Materials, Macau University of Science and Technology, Taipa 999078, Macao Special Administrative Region of China

ARTICLE INFO

ABSTRACT

Photocatalytic overall water splitting represents a promising strategy to achieve the renewable hydrogen energy. Although $Cd_{1-x}Zn_xS$ catalysts show high photocatalytic hydrogen evolution efficiency in pure water, severe photocorrosion problems limit their applications. Herein, photocatalytic system composed of Co_3O_4 nanoparticles anchored one-dimensional $Cd_{0.6}Zn_{0.4}S$ nanorods (CZS/Co_3O_4) is designed and prepared by a simple hydrothermal method. Transient photovoltage tests and continuous wavelet transform analyses demonstrate that Co_3O_4 nanoparticles efficiently capture the photogenerated holes to inhibit photocorrosion of CZS nanorods, accelerate surface charge transfer and prolong the lifetime of photogenerated carriers. The CZS/Co_3O_4 photocatalyst exhibits high H_2 and O_2 evolution rates of 83.48 and 40.48 μmol h^{-1} g^{-1}, respectively. The stability is maintained over four reaction cycles without significant decrease in the absence of sacrificial agents. This work provides insight into metal sulfides against photocorrosion and extends the range of metal sulfides in solar water splitting.

1. Introduction

Photocatalytic decomposition of water by semiconductors for hydrogen evolution reaction (HER) has emerged as a desirable technology to solve the global energy demands and environmental issues.[1] Although innumerable semiconductor photocatalysts have been used in photocatalytic HER during the past decades, efficient photocatalytic semiconductors still encounter several challenges, such as poor light response and weak surface/interface electronic transport. In the past several decades, $Cd_xZn_{1-x}S$ (CdZnS) has intrigued enormous scientific attention due to its suitable band gap and visible light absorption capacity.[2] However, pristine CdZnS catalysts are generally weak in structural stability caused by serious photocorrosion under long-time irradiation, seriously affecting their photocatalytic performance.[3–5] In this scenario, hole sacrificial agents (methanol, lactic acid and triethanolamine, etc.) have been often added into the reaction system to consume photogenerated holes, thus increasing the survival time of photogenerated electrons and inhibiting the photocorrosion for reduction half reaction to produce hydrogen.[6,7] Unfortunately, partial solar

energy is consumed in chemical reactions caused by the hole sacrificial agents, which is not energy saving and environmental protection. Therefore, hydrogen production stored in the hole scavengers can only regarded as sources of "partial solar fuel".[8] Based on rapid transfer or consumption of holes in CdZnS during photocatalytic process, the spatial separation of charge carriers is the key to solving the above problems.

In recent years, researchers have mainly focused on the processes of cocatalyst development to design novel photocatalytic systems, in order to obtain efficient photocatalytic overall water splitting.[9–11] The cocatalyst loading can reduce the overpotential, provide effective surface reaction active sites on the semiconductor surface and contribute to the rapid separation of photogenerated carriers at the cocatalyst/semiconductor interface. In addition, oxide cocatalysts can effectively protect the metal sulfide from photocorrosion.[12] Most efficient cocatalysts are based on precious metals, such as Pt, Pd, IrO_2 and RhO_x.[13–15] Considering the scarcity and high price of noble metals and the need for large-scale applications, there is an urgent need to develop economical and high-activity non-noble metal-based cocatalyst. For example, Xu et al. proposed the modification of $Zn_{0.5}Cd_{0.5}S$ with

---

MCo_2O_4 spinels, which improved water splitting to H_2 in absence of Na_2S/Na_2SO_3.[16] Lu et al. constructed the CdS nanoparticles modified with chemical inert Al_2O_3 shell, which significantly improved the photostability of CdS during photocatalytic water splitting.[17] Among these cocatalysts, tricobalt tetraoxide (Co_3O_4) has been demonstrated as superior cocatalyst for improving the photocatalytic activity of host semiconductors. It serves as hole collector to effectively separate electron-hole pairs and as oxidative cocatalysts for photocatalytic oxygen evolution. In addition, appropriate electron sink function and low hole transfer overpotential make it easy to integrate well with other semiconductors.[18–20] Liu et al. proved that Co_3O_4 quantum dots change the work function of TiO_2, promoting the electron transfer from TiO_2 to Co_3O_4 quantum dots.[21] Combining with above analysis, we expect that the metal oxide cocatalysts deposited on the CdZnS can effectively divert holes from the sulfide to the oxidation catalyst site, thus effectively regulating the spatial motion of holes and addressing the stability issue of Cd-based chalcogenide photocatalysts.

In this study, Co_3O_4 nanoparticles as a cocatalyst are successfully anchored onto CdZnS nanorods (CZS/Co_3O_4) via a simple hydrothermal route. Under visible light irradiation, the optimized CZS/Co_3O_4 photocatalyst exhibits remarkable photocatalytic performance and stability without sacrificial agents in pure water, which was attributed to the loading of Co_3O_4 nanoparticles that not only facilitated the transfer of photogenerated holes, but also restricted the electron-hole recombination. This work presents a facile strategy to protect the photosensitive semiconductors from photocorrosion, and offers a new insight for designing highly stable and efficient catalysts for solar energy conversion.

2. Experimental section

2.1. Synthesis of CdS, ZnS and CZS nanorods

First, $Cd(NO_3)_2 \bullet 4 H_2O$ (1.8 mmol), $Zn(NO_3)_2 \bullet 6 H_2O$ (1.2 mmol) and NH_2CSNH_2 (9.0 mmol) were dissolved in 30 mL of the mixture of $C_2H_8N_2$ and deionized (DI) water (v:v = 2:1) and stirred for 30 min, and transferred into 50 mL Teflon–lined stainless–steel autoclaves, sealed maintained at 180 °C for 12 h. After cooling to room temperature, the precipitates were washed several times with DI water and ethanol and the yellow powder was obtained after drying in a vacuum oven at 70 °C overnight. Bulk phases of CdS and ZnS were synthesized using the same procedure mentioned above with different raw materials.

2.2. Synthesis of Co_3O_4 nanoparticles-anchored CZS nanorods photocatalysts

The preparation of Co_3O_4 nanoparticles-anchored CZS nanorods photocatalysts was realized through a one-step solvothermal method. Typically, 200 mg CZS nanorods were dissolved in the mixed solution of ethylene glycol (20 mL) and DI water (12.5 mL) with ultrasonically treating for 30 min. A specified amount of $Co(NO_3)_2 \cdot 6 H_2O$ was added to the above suspension under stirring and then 25 wt% $NH_3 \cdot H_2O$ was added to adjust pH to 9. The mixed suspension was then transferred into a 50 mL Teflon–lined autoclave and heated at 160 °C for 6 h. The dark-yellow precipitate was separated by centrifugation and washed with ethanol and DI water for three times. Finally, the obtained product was dried in a vacuum oven at 60 °C overnight. By controlling the amount of $Co(NO_3)_2 \cdot 6 H_2O$, the mass ratio of Co_3O_4 nanoparticles to CZS nanorods was 0.01, 0.03 and 0.05 and the as-prepared samples were labeled as, CZS/Co_3O_4-x (x = 1, 3, 5). In addition, pure Co_3O_4 nanoparticles were prepared similarly without the introduction of CZS nanorods.

3. Results and discussions

3.1. Morphology analysis and Structural characterization

The morphology and structure of as-prepared CZS nanorods, Co_3O_4 nanoparticles and CZS/Co_3O_4-3 composites were characterized using scanning electron microscopy (SEM) and transmission electron microscope (TEM) measurements. CZS solid solution was found to be the typical one-dimensional nanorod-like morphology with a smooth surface (Fig. 1a). The prepared Co_3O_4 shows nanoparticle morphology and the average diameter is 30–50 nm (Fig. S2). The high-resolution TEM (HRTEM) image of CZS shows the lattice fringe spacing of 0.29 nm, corresponds to the (1 0 1) plane of CZS (Fig. 1b).[22] After loading of the Co_3O_4 nanoparticles, there is no obvious morphology change of CZS/Co_3O_4-3 as shown in the SEM images (Fig. S3), which is still the nanorod morphology with the width of 30 nm and the length of approximately 300 nm. As given from the TEM image in Fig. 1c, it can be seen that small size Co_3O_4 nanoparticles were tightly anchored on the surface of CZS nanorods, indicating the intimate connection between Co_3O_4 nanoparticles and CZS nanorods. It is well-known that Co_3O_4 nanoparticles are useful to gather holes and the unique structure of CZS/Co_3O_4-3 photocatalyst facilitates the effective separation of photogenerated electron-hole pairs, leading to the improvement of photocatalytic performance.[20] The HRTEM image of CZS/Co_3O_4-3 (Fig. 1d) clearly reveals the connected crystal lattices of 0.32 nm representing to the (0 0 2) planes of the CZS nanorods, and the wurtzite CZS nanorods grow along [0 0 1] direction.[22] Furthermore, the presence of Co_3O_4 nanoparticles at surfaces of CZS is confirmed by the HRTEM image (Fig. 1d), in which the lattice spacing of 0.20 nm is ascribed to the (4 0 0) plane of Co_3O_4 nanoparticles.[23] The HAADF-STEM image and energy-dispersive spectra (EDS) element mapping results (Fig. 1e-j) further confirms that Cd, Zn, S, Co and O elements are homogeneously dispersed in CZS/Co_3O_4-3, confirming that the CZS/Co_3O_4-3 composites were synthesized successfully.

The phase structure of as-prepared CZS nanorods and CZS/Co_3O_4-x samples were characterized by X-ray diffractometer (XRD). The actual Cd: Zn molar ratio of CZS solid solution is 0.58: 0.40 as confirmed by inductively coupled plasma (ICP) test. The characteristic peaks of the CdS and ZnS (Fig. S4) are well-matched with the hexagonal ZnS (PDF# 02–1310) and hexagonal CdS (PDF# 41–1049).[24] The XRD patterns of CZS exhibits the hexagonal phase with clear shifts to the high angle side, in comparison with the CdS, which demonstrates that the CZS were Zn-doped CdS instead of the mixtures of CdS and ZnS (Fig. 2a).[24] For the XRD pattern of pure Co_3O_4 nanoparticles (Fig. S5), the characteristic peaks match well with cobalt oxide (PDF# 42–1467).[25] However, no characteristics belonging to Co_3O_4 nanoparticles were observed for CZS/Co_3O_4-3 composites (Fig. 2a), and the same was observed for other CZS/Co_3O_4-x composites (Fig. S5), possibly due to the low loading amount of the Co_3O_4.

The X-ray photoelectron spectroscopy (XPS) was further investigated to determine the surface chemical state and the chemical composition of Co_3O_4, CZS and CZS/Co_3O_4-3 composites. In the XPS full spectra (Fig. S6), peaks of Cd, Zn, S and Co could be observed for the CZS/Co_3O_4-3 composites. The binding energies of Cd 3d (404.4 and 411.2 eV) and Zn 2p (1021.2 and 1044.3 eV) for CZS are shown in Fig. 2b and c, which correspond to the Cd^{2+} and Zn^{2+} valence states, respectively.[26] The S 2p spectrum of CZS indicates two peaks at 160.8 and 162.0 eV were attributed to $2p_{3/2}$ and $2p_{1/2}$ of S^{2-} in CZS (Fig. 2d). [26] After loading Co_3O_4 to CZS, the Cd, Zn, and S peaks in the CZS/Co_3O_4-3 composites shift to higher energies compared to those peak positions in CZS. The difference in binding energies is always related to the surface electron density, which reveals the electron transfer from CZS with high Fermi energy (E_f) of to Co_3O_4 with lower E_f. [27] The electrons transfer from CZS to Co_3O_4 across the CZS/Co_3O_4 interface during the complexation process, leading to increased electron concentration in Co_3O_4 resulting in the strong interaction between CZS
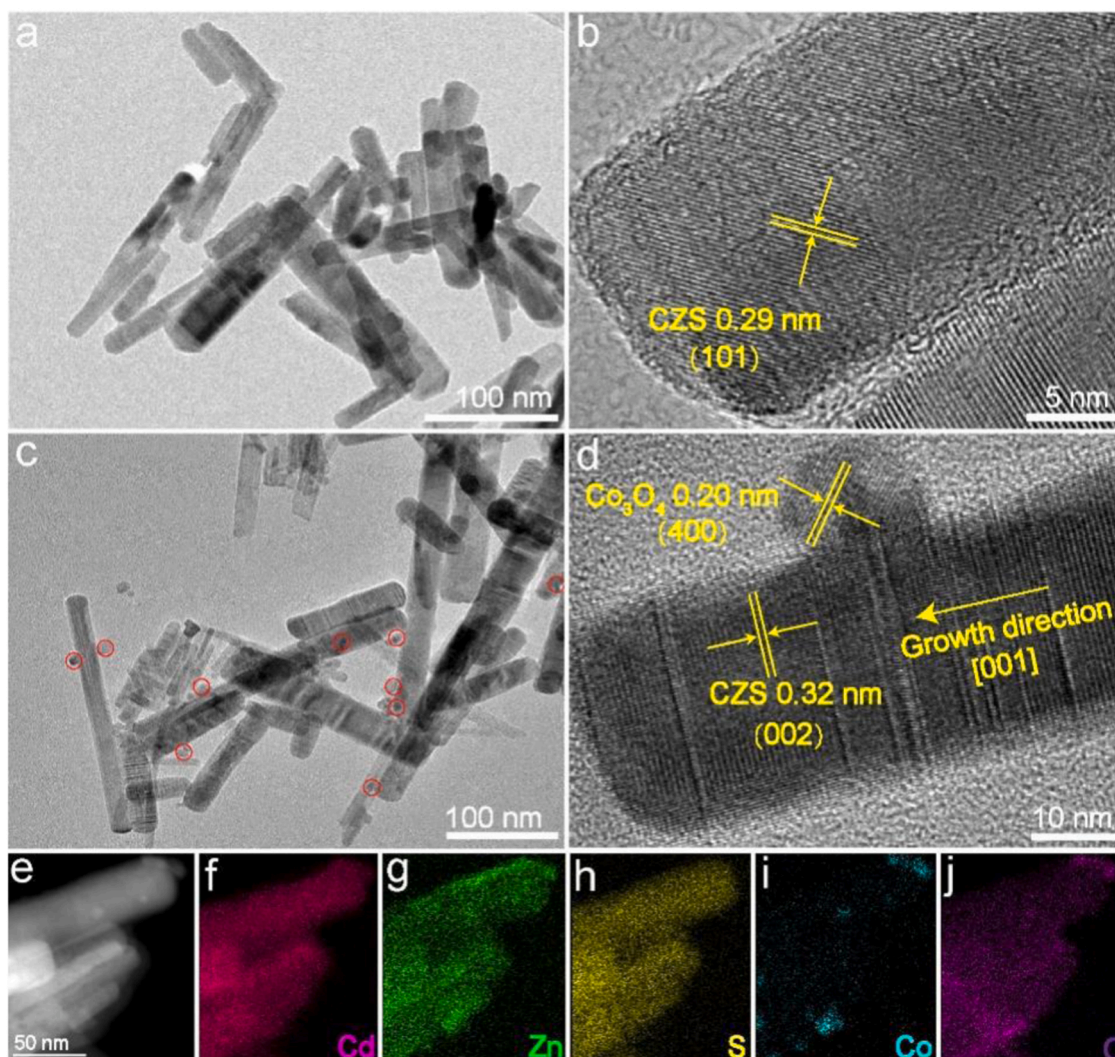
Fig. 1. (a) TEM and (b) HRTEM images of CZS, (c) TEM and (d) HRTEM images of CZS/Co$_3$O$_4$-3, (e-i) HAADF-STEM and element mapping of CZS/Co$_3$O$_4$-3.

and Co$_3$O$_4$. Correspondingly, two peaks at 780.2 and 795.3 eV were observed in the Co 2p spectrum of CZS/Co$_3$O$_4$-3 (Fig. 2e), which could be consigned to the Co 2p$_{3/2}$ and Co 2p$_{1/2}$ of Co$_3$O$_4$, respectively.[28] In the O 1 s region of CZS/Co$_3$O$_4$-3 (Fig. 2f), the peaks at 530.0, 531.3, 533.0 eV are related to the Co-O bonds, hydroxyls, and bound H$_2$O of hydration, respectively.[28] For Co$_3$O$_4$, as shown in Fig. S7a, the O 1 s spectra emerge two palpable peaks at 780.9 and 796.4 eV, related to Co 2p$_{3/2}$ and Co 2p$_{1/2}$.[29] In the O 1 s region, there were three characteristic peaks that appeared at 529.8, 531.2 and 532.9 eV, as shown in Fig. S7b, which were derived from Co-O, hydroxyls, and bound H$_2$O of hydration, respectively.[29] Therefore, the combined XRD, SEM, TEM and XPS results clearly proved the successful hybridization of Co$_3$O$_4$ nanoparticles with CZS nanorods.

3.2. Optical properties and energy level structure

The optical properties of the samples were evaluated using UV–vis diffuse reflectance spectra (UV–vis DRS). The pristine CZS nanorods have an absorption edge at about 530 nm and Co$_3$O$_4$ nanoparticles manifest intense light absorption from 300 to 800 nm as shown in Fig. 3a. After further depositing of Co$_3$O$_4$ nanoparticles, the light absorption of CZS/Co$_3$O$_4$-3 composite is significantly increased in the visible light region compared with that of the CZS nanorods, indicating the enhanced photoabsorption ability, which is attributed to the black color of Co$_3$O$_4$ nanoparticles. The absorption edge of CZS/Co$_3$O$_4$-3

exhibits a distinct red-shift compared with CZS nanorods, suggesting that the presence of Co$_3$O$_4$ leads to significant high scattering over the long wavelength range.[11] According to Kubelka-Munk method, the $(\alpha h\nu)^2$ is plotted versus the photon energy (hν) (CZS is direct-gap semiconductor) as shown in Fig. 3b.[30] By extrapolating the plot to $(\alpha h\nu)^2 = 0$, the band gap (E$_g$) values of CZS is estimated as 2.37 eV. Generally speaking, the band gap of the composite cannot be directly calculated by Kubelka-Munk method, but because of low loading amount of Co$_3$O$_4$ nanoparticles in the CZS/Co$_3$O$_4$-x composites, and Co$_3$O$_4$ with full spectrum (300–800 nm) absorption phenomenon, the band gap of CZS/Co$_3$O$_4$-3 can be roughly estimate to be 2.35 eV. Notably, the small differences in the band gap values of samples indicate that they have similar light absorption behavior. The band structure of CZS and Co$_3$O$_4$ are determined by the Mott-Schottky plots, which were recorded in dark as illustrated in Fig. 3c and S8.[31] The Mott-Schottky plots of CZS show positive values indicate its n-type semiconductor properties, while negative slopes for Co$_3$O$_4$ indicate the typical p-type semiconductor characteristics.[32] The flat-band potential (E$_{fb}$) can be determined by the Mott-Schottky plots and the flat band potential corresponds to Fermi level. The E$_{fb}$ of CZS and Co$_3$O$_4$ are estimated to be − 0.92 V and 1.03 V vs. Ag/AgCl. The conduction band position (E$_{CB}$) of n-type semiconductors was negative by about 0.1 V or 0.2 V over the E$_{fb}$ value, while the value band position (E$_{VB}$) of p-type semiconductors was positive by about 0.1 or 0.2 V over the E$_{fb}$ value.[33] That is to say, the E$_{CB}$ of CZS is calculated to be − 1.12 V vs. Ag/AgCl, which is − 0.92 vs.
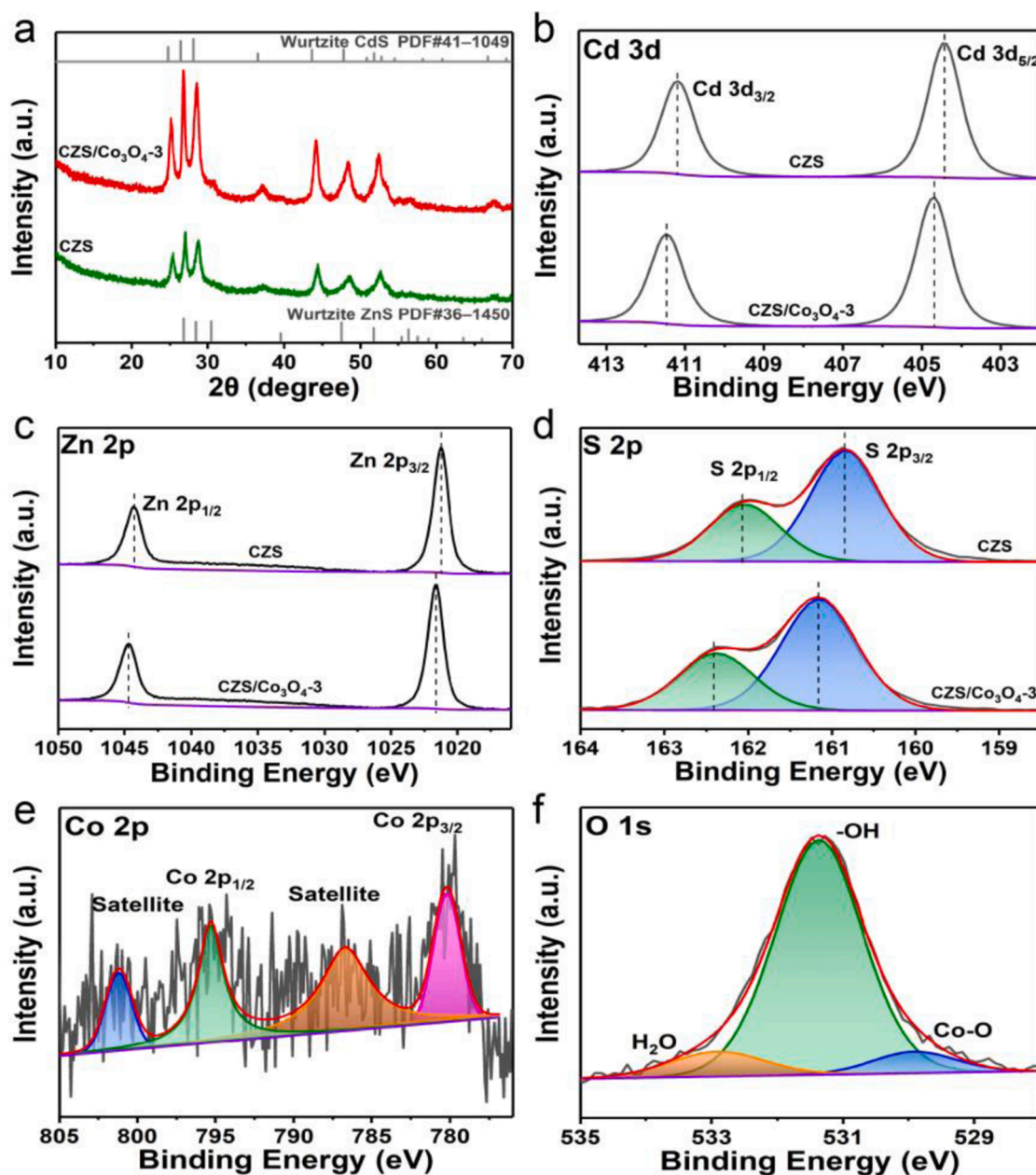
Fig. 2. (a) XRD patterns of CZS and CZS/Co$_3$O$_4$-3; High-resolution XPS spectra of (b) Cd 3d, (c) Zn 2p and (d) S 2p for CZS and CZS/Co$_3$O$_4$-3, (e) Co 2p and (f) O 1 s for CZS/Co$_3$O$_4$-3.

NHE (E$_{NHE}$ = E$_{Ag/AgCl}$ + 0.19 V), respectively. Thus, the valence band value of CZS is 1.45 V vs. NHE, according to E$_{VB}$ = E$_{CB}$ + E$_g$. Therefore, the band structure of CZS/Co$_3$O$_4$ can be summarized and shown in Fig. 3d. Meanwhile, to further determine the valence band potentials, the XPS-VB spectrum of CZS is shown in Fig. S9. According to the Mulliken electronegativity theory, the valence bands of CZS is near 1.43 V vs. NHE, which is consistent with the above calculation results. [34].

3.3. Photocatalytic performances for overall water splitting

The visible light-driven photocatalytic overall water splitting performances were evaluated under in the absence of any sacrificial reagents or noble metals. The H$_2$ and O$_2$ generation rates for pristine CZS nanorods achieve 20.46 and 9.65 μmol h^{-1} g^{-1} with molar proportion of 2 to 1(Fig. 4a and S10), which should be attributed to the optimized band structure and charge separation efficiency compared to pristine

ZnS and CdS. While for Co$_3$O$_4$ nanoparticles, it shows negligible H$_2$ and O$_2$ production activity because of the fast recombination of photogenerated carriers. Furthermore, even with a low introduced amount of Co$_3$O$_4$ (1%), CZS/Co$_3$O$_4$-1 exhibited a significant enhancement of the catalytic activity, the H$_2$ and O$_2$ production rate of CZS/Co$_3$O$_4$-1 elevates up to 32.12 and 15.21 μmol h^{-1} g^{-1}, respectively. With increasing Co$_3$O$_4$ content up to 3%, the H$_2$ evolution rate of CZS/Co$_3$O$_4$-3 can be remarkably improved and reach up to 83.48 μmol h^{-1} g^{-1}, and O$_2$ evolution proceeds continuously at a rate of 40.48 μmol h^{-1} g^{-1}. The H$_2$ production with different catalyst concentrations is shown in Fig. S11. The significant increase in photocatalytic activity of the CZS/Co$_3$O$_4$-3 can be partly attributed to the cooperative effect of the Co$_3$O$_4$ nanoparticle cocatalysts and CZS nanorods, which facilitate the separation of photogenerated charge carriers compared to CZS nanorods. However, when the Co$_3$O$_4$ content was 5%, decrease of the H$_2$ and O$_2$ evolution rates were observed, which may be due to the partial shielding of light absorption and active sites on the CZS. The wavelength dependent
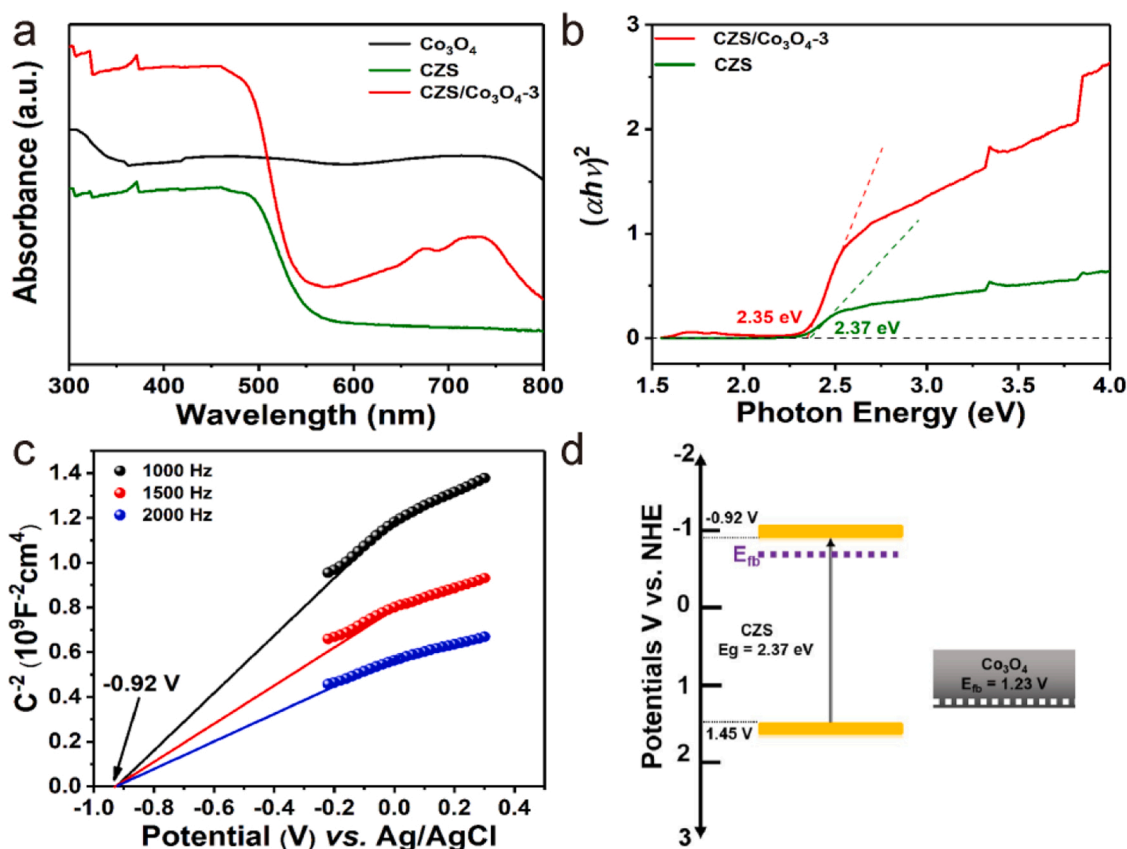
Fig. 3. (a) UV–vis DRS of Co_3O_4, CZS and CZS/Co_3O_4-3, (b) The corresponding $(\alpha h\nu)^2$ versus hν curves of CZS and CZS/Co_3O_4-3, (c) Mott-Schottky plots of CZS, and (d) Band structure of CZS/Co_3O_4-3.

apparent quantum yield (AQY) of CZS/Co_3O_4-3 were obtained to at various wavelengths (Fig. 4b). Encouragingly, the AQY at 365 nm and 420 nm arrive at 2.94% and 1.22%, respectively. Compared with related metal sulfide photocatalysts for hydrogen production (Table S1), the photocatalytic activity of our CZS/Co_3O_4-3 surpasses most reported photocatalysts, showing the great potential of solar water splitting for future work.

Furthermore, recycling tests on both CZS and CZS/Co_3O_4-3 were also conducted to study the stability of the catalysts. As illustrated in Fig. 4c, the CZS/Co_3O_4-3 maintains excellent photocatalytic H_2 evolution activity and shows no obvious decrease in a total of 20 h with each run of 5 h. Based on previous literature research, an induction period was observed at the early stage of the photocatalytic reaction.[35] In this process, the catalyst is further activated. Therefore, the hydrogen production of the second cycle is larger than that of the first cycle. To testify the role of Co_3O_4 nanoparticles in CZS/Co_3O_4-3, the corresponding photocatalytic performance have been carried out. It can be observed that the hydrogen production rate of CZS nanorods decreases quickly and only 51.2% of initial performance is preserved after four cycles. The reason is that the confinement effect of Co_3O_4 can hinder the photogenerated hole from accumulating on the CZS to stable CZS by suppress the photocorrosion process, whereas the pristine CZS suffered from severe photocorrosion. In order to verify the photocorrosion resistance, the concentration of Cd^{2+} ions in the catalyst dispersion was determined by ICP method. As shown in Table S2, it was found that high Cd^{2+} concentrations were observed in the photocatalysis system using CZS. However, there is only negligible Cd^{2+} in the CZS/Co_3O_4-3 sample after four cycles. Impressively, there was no noticeable morphological and crystal structure change of the CZS/Co_3O_4-3, as verified by the XRD, SEM and TEM image, indicating the superior catalytic stability without obvious photocorrosion (Fig. 4d and Fig. S12). In addition, based on the

XPS results in Fig. S13, the Co and O species associated with Co_3O_4 were preserved in the used CZS/Co_3O_4-3, which evidences the stability of CZS/Co_3O_4-3 sample.

3.4. Exploration of photogenerated charge separation and transfer

A series of photoelectrochemical measurements were carried out to explore the influence of Co_3O_4 nanoparticles in the regulation of photogenerated charge behavior for CZS/Co_3O_4-3. In Fig. 5a, CZS/Co_3O_4-3 exhibits a much higher photocurrent density than CZS nanorods and Co_3O_4 nanoparticles, indicating that the photoinduced carriers separation and transfer is significantly improved by the introduction of Co_3O_4 nanoparticles. And the corresponding arc radiuses on the electrochemical impedance spectroscopy (EIS) spectra are presented in Fig. 5b. Thereinto, CZS/Co_3O_4-3 displays the smallest diameter compared to CZS nanorods and Co_3O_4 nanoparticles, revealing the faster interfacial charge transfer property and lower interfacial charge transport resistance. Furthermore, the curves of the linear sweep voltammetry (LSV) (Fig. 5c) show that CZS/Co_3O_4-3 has the lowest overpotential, demonstrating enhanced electron transport efficiency for the HER. It must be accepted that the photocatalytic HER activity largely based on the overpotential of H_2 production reaction, so CZS/Co_3O_4-3 has excellent photocatalytic hydrogen evolution performance. Time resolved photoluminescence (TRPL) analysis further revealed the migration dynamics of photo-generated charge carriers and lifetime of the CZS/Co_3O_4-3 photocatalyst. As depicted in Fig. 5d, the average lifetime is obtained through a quadratic exponential function fitting (relevant data are presented in Table S3). The average PL lifetime of CZS and CZS/Co_3O_4-3 are reached to 1.10 ns and 3.36 ns, respectively. The longer fluorescence lifetime of CZS/Co_3O_4-3 indicates the recombination of photogenerated charges have been suppressed with the aid of the efficient and rapid hole
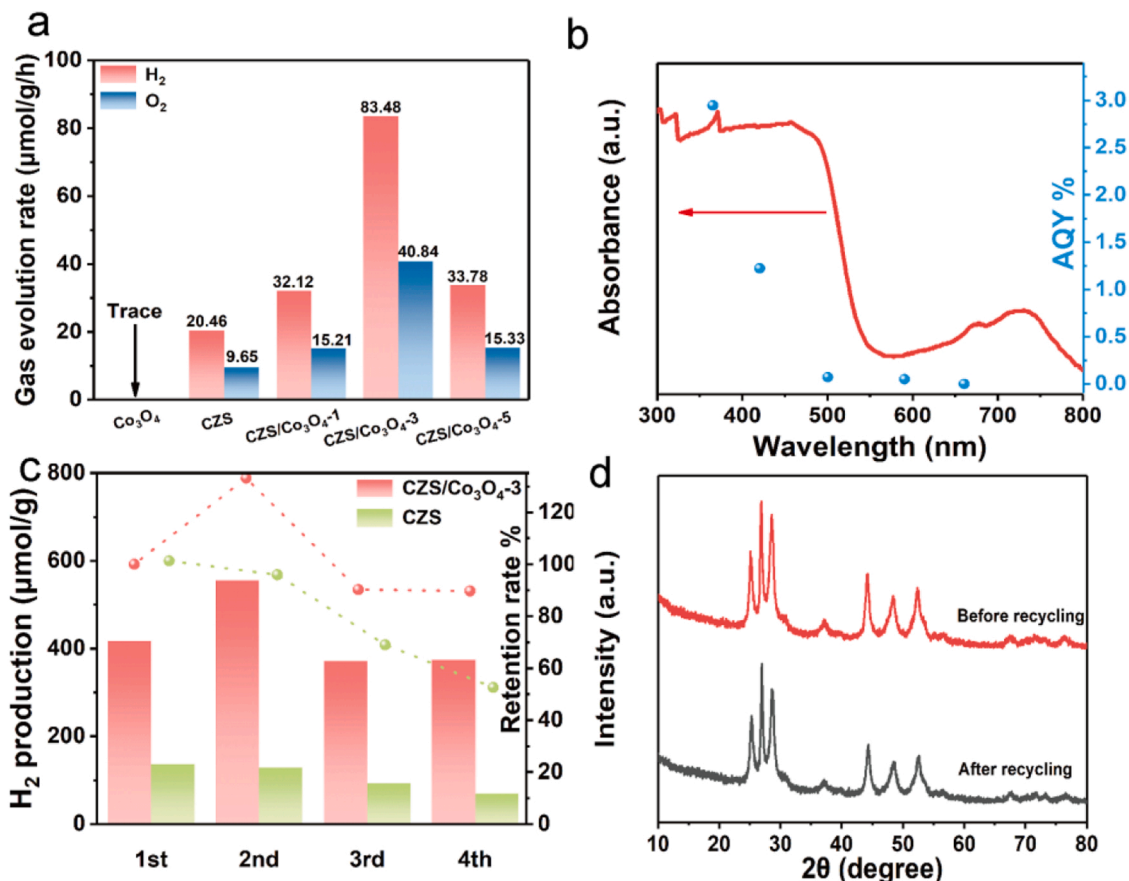
Fig. 4. (a) Photocatalytic overall water splitting of Co_3O_4, CZS and CZS/Co_3O_4-x, (b) UV–vis DRS and wavelength-dependent AQY of photocatalytic H_2 generation over CZS/Co_3O_4-3, (c) cyclic stability experiments of CZS and CZS/Co_3O_4-3, and (d) XRD patterns of fresh and used CZS/Co_3O_4-3.

trapping by Co_3O_4 nanoparticles. Therefore, the above results demonstrate that the CZS nanorods anchored with well-dispersed Co_3O_4 nanoparticles can effectively suppress recombination of photogenerated electrons and holes and accelerate the transferring of photo-generated electrons, then enhance the corresponding photocatalytic performance. In order to understand the spatial separation behavior of photogenerated carriers in CZS/Co_3O_4-3, oxidation of Mn^{2+} with IO_3^- as hole collectors were carried out. The deposition sites of MnO_x nanosheets on Co_3O_4 part were marked by HRTEM (Fig. S14), which reveals the photogenerated holes are inclined to accumulate on Co_3O_4 sites for oxidation reaction.

The transient photovoltage (TPV) tests were conducted to further study the charge transfer mechanism under light excitation and the schematic diagram of test device is shown in Fig. S15.[36–38] The photovoltage intensity of CZS/Co_3O_4-3 is the highest as shown in Fig. 6a, indicating Co_3O_4 promotes the separation and transfer efficiency of photogenerated charge, which is conducive to photocatalytic activity. Additionally, small t_{max} (the time required for peak intensity to reach a maximum valve) means fast charge extraction process.[39] As shown in Fig. 6b, the t_{max} of CZS/Co_3O_4-3 (t_{max3}) is less than that of CZS (t_{max2}) and Co_3O_4 (t_{max2}), testifying the fast electron transmission rate of CZS/Co_3O_4-3. The Co_3O_4 nanoparticles anchored on the CZS nanorods, facilitates electron transfer to the steady state. The integral area of shadow part A represents the maximum amount of electrons extracted from the sample, namely the extraction efficiency of the charge extraction process.[40] At the same time, Fig. 6c shows the enlarged diagram of the charge extraction process in the TPV curve and the corresponding integral region. The A_1 (0.076) of CZS is slightly larger than that of CZS/Co_3O_4-3 (A_3, 0.067), much larger than that of Co_3O_4 (A_2, 0.058), revealing that CZS generate more photogenerated electrons.

The electron decay constant (τ) related to charge recombination. It shows that the recombination of photogenerated electrons and holes process of CZS/Co_3O_4-3 (τ_3 = 0.455 ms) is slower than CZS (τ_2 = 0.349 ms) and Co_3O_4 (τ_1 = 0.342 ms) (Fig. 6d). The above analyses demonstrate that Co_3O_4 nanoparticles anchored on the surface of CZS nanorods can effectively promote the extraction of charge. As a typical oxidation co-catalyst, Co_3O_4 has a prominent hole capturing effect. More electrons preferable transport to the surface of CZS nanorods, so that the incidence of charge recombination is slightly reduced and the charge life is prolonged. It is noteworthy that there is a sharp peak at the beginning in the TPV curve of CZS, but that is not observed in the other samples. The CZS nanorods have partially stacking faults on the surface, resulting in rapid charge redistribution during laser irradiation in a short time. [41] The spike disappeared when the Co_3O_4 nanoparticles anchored on the CZS nanorods, which may be attributed to the fact that Co_3O_4 can act as hole-trap sink and transfer them uniformly at the CZS/Co_3O_4-3 interface, leading to the prolong lifetime. The one-dimensional CZS nanorod with appropriate diameter ratio can effectively facilitate the directional transport of charges, shorten charge transfer distance to the surface, and excite more charges to the surface. But a large number of electron-hole pairs recombined in a short time due to surface defects of CZS nanorod, resulting in few effective charges involved in the photocatalytic reaction. To further understand the effect of Co_3O_4, the number of the surface effective charges or the number of charges that remains on the surface after charge extraction and recombination ($A_{eff} = A^*\tau/t_{max}$) of the composite material is further calculated.[42] As shown in Fig. S16, it is obvious that the CZS/Co_3O_4-3 has a much higher A_{eff} number (0.05) than those of Co_3O_4 (0.03) and CZS (0.04), implying that more surface electrons-hole pairs were involved in photocatalytic reactions after introducing Co_3O_4.
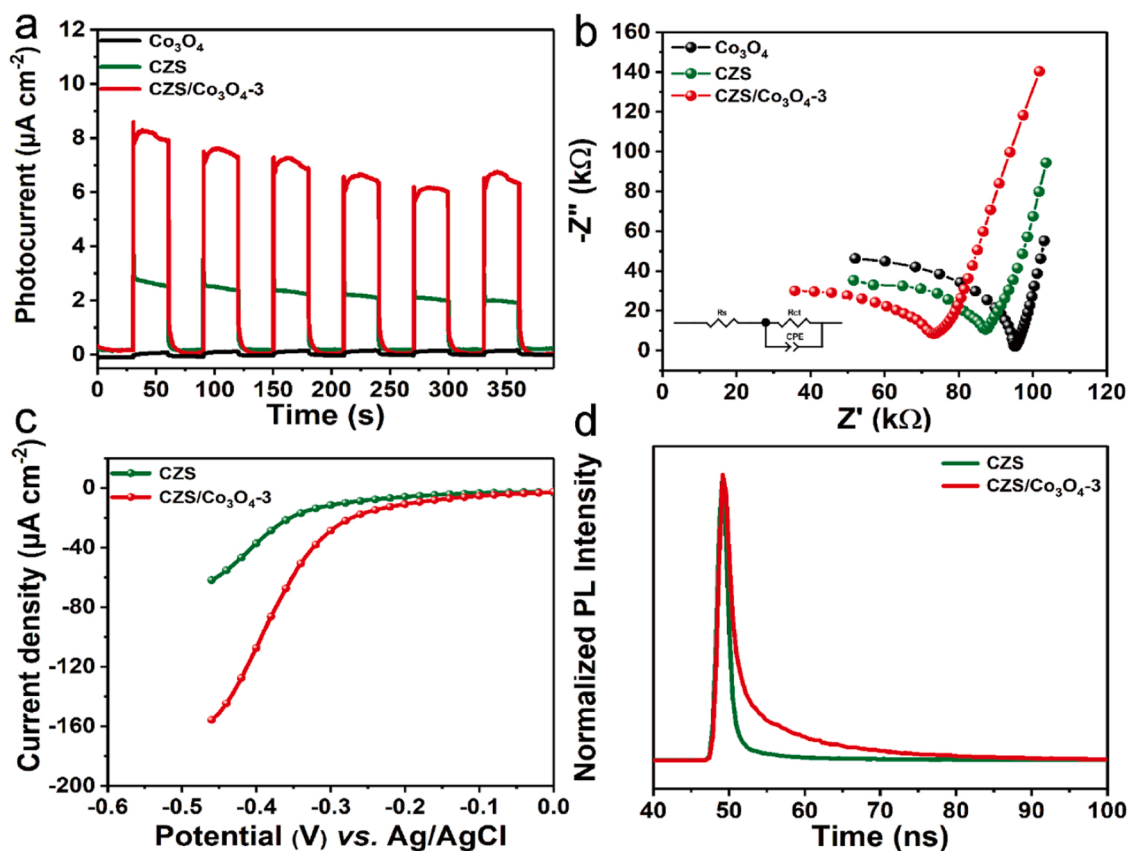
Fig. 5. (a) Photocurrent responses, (b) EIS Nyquist plots for Co_3O_4, CZS and CZS/Co_3O_4-3, (c) LSV curves, and (d) TRPL spectra of CZS and CZS/Co_3O_4-3.
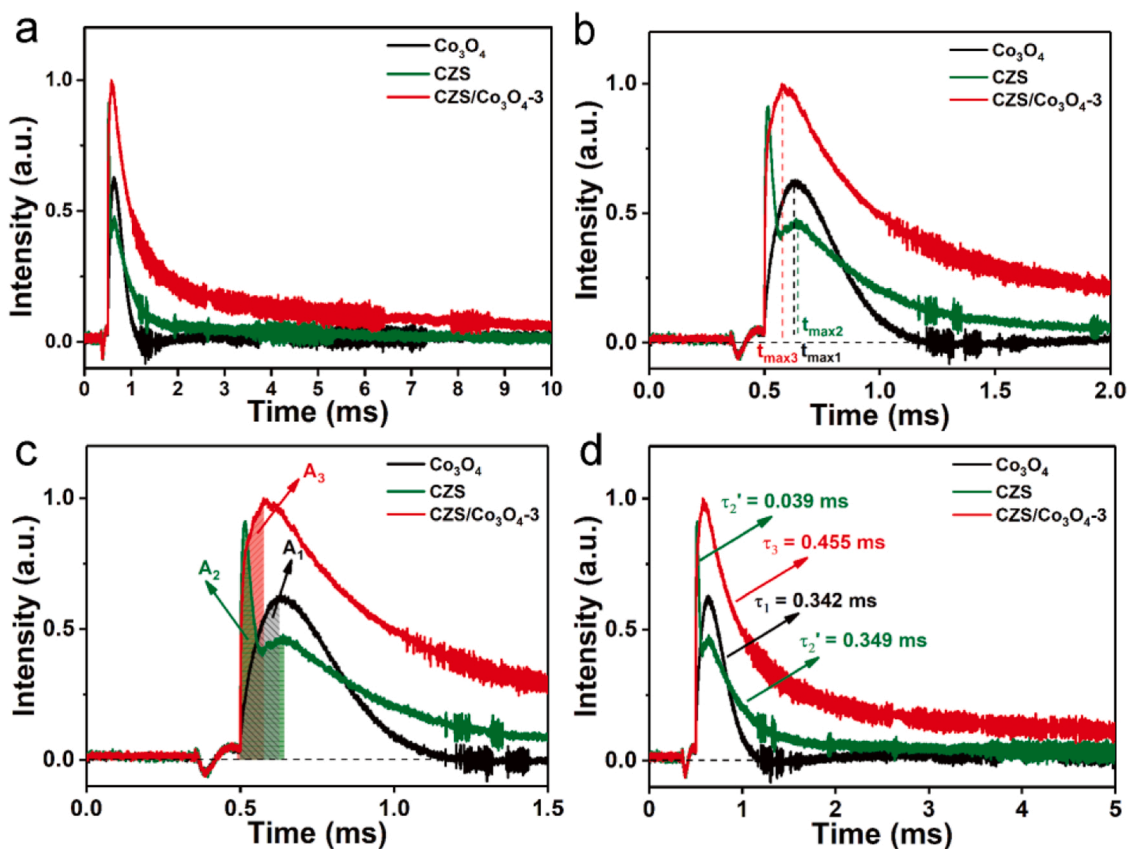

Fig. 6. (a) TPV curves, (b) maximum charge extraction time (t_{max}), (c) charge extraction process (A), (d) attenuation constants (τ) of Co_3O_4, CZS and CZS/Co_3O_4-3.

The internal charge behaviors including the separation and dynamic information were investigated by fast Fourier transform (FFT) and continuous wavelet transform (CWT). FFT is a tool for decomposing a waveform (a function or signal) into an alternating representation with sine and cosine characteristics. The TPV relaxation signals of CZS, Co_3O_4 and CZS/Co_3O_4-3 have a very smooth curve with no visible peak, indicating that there are no evident static or periodic frequency components. The curve characteristics of TPV signal and FFT results show that the TPV curve has obvious non-static characteristics (Fig. 7a). As the FFT can only detect the frequency components of these signals, it is not possible to determine when they are present. Therefore, using CWT to convert non-stationary TPV curves to frequency-scale/time-scale, 2D spectra of samples are shown in Fig. 7b and Fig. S17. In order to investigate the behavior of electrons at different frequencies, the intensity of the peaks positions at different frequencies (10, 20, 30, 40, 50, 60, 70 and 80 Hz) was compared in relation to time. At low frequencies of 10, 20 and 30 Hz, it represents a relatively slow electron transfer process (Fig. 7c and Fig. S18a-b). After the introduction of Co_3O_4, the delay time difference can be ascribed to the ability of Co_3O_4 to store charges, thereby prolonging the lifetime of electron-hole pairs at low frequencies. And in the high frequency scale (>30 Hz) region, the peak position of CZS/Co_3O_4-3 is in front of CZS, which accounts for the excellent electron transport ability of Co_3O_4 at high frequencies (Fig. S18b-d). The time difference (Δt: $t_2 - t_1$) of peak values between CZS/Co_3O_4-3 and CZS were calculated (Fig. 7d), which are 0.081, 0.019, 0.000, -0.004, -0.005, -0.006, -0.009 and -0.011 ms at 10, 20, 30, 40, 50, 60, 70 and 80 Hz, respectively, indicating that Co_3O_4 makes the slow process slower and the fast process faster.[43,44] Based on all above results, Co_3O_4 with the charge storing ability prolongs the lifetime of low-frequency electrons, accelerate the transport of high-frequency charges, and suppress the recombination of electron-hole pairs for CZS/Co_3O_4-3.

3.5. Photocatalytic mechanism

As shown in Fig. S19, the number of electron transfers (n) for CZS/Co_3O_4 was determined to be 4 via the i-t curves on the rotating disk-ring electrode (RRDE), which indicates that the photocatalytic water splitting process of CZS/Co_3O_4 is a typical 4-electron pathway under visible light irradiation. In addition, H_2O_2 was not detected via the UV–vis spectrophotometry test, further confirming the $4e^-$ process oxygen generation of the photocatalytic water splitting (Fig. S20).

On the basic of the above results, the schematic diagrams to elucidate the potential photocatalytic mechanism for CZS/Co_3O_4 is proposed as shown in Fig. 8. According to the result of Mott-Schottky and XPS results, CZS is an n-type semiconductor, while Co_3O_4 is a p-type semiconductor. The Fermi level of n-type semiconductors approaches the conduction band (CB), while the Fermi level of p-type semiconductors approaches the valence band (VB) (Fig. 8a). Different energy levels between CZS and Co_3O_4 lead to the diffusion of electrons from the CZS to the Co_3O_4 and the holes of Co_3O_4 prefer to diffuse into CZS until the Fermi levels of CZS and Co_3O_4 achieve an equilibrium in darkness (Fig. 8b).[45] During the migration of electrons through the CZS/Co_3O_4 interface, the interface region near CZS is positively charged owing to the loss of electrons, which leads to the formation of an electrondepletion layer of and the upward bending of band edge of CZS.[46] Therefore, an internal electric field (IEF) is established at the interfaces of CZS and Co_3O_4. Under visible-light excitation, CZS nanorods are excited to produce the electron-hole pairs (Fig. 8c). Driven by IEF, abundant holes tend to transfer to Co_3O_4 due to trapped effect, while more photo-electrons in the CB of CZS nanorods accumulate, which facilitates charge carrier separation and prevents the photocorrosion. In
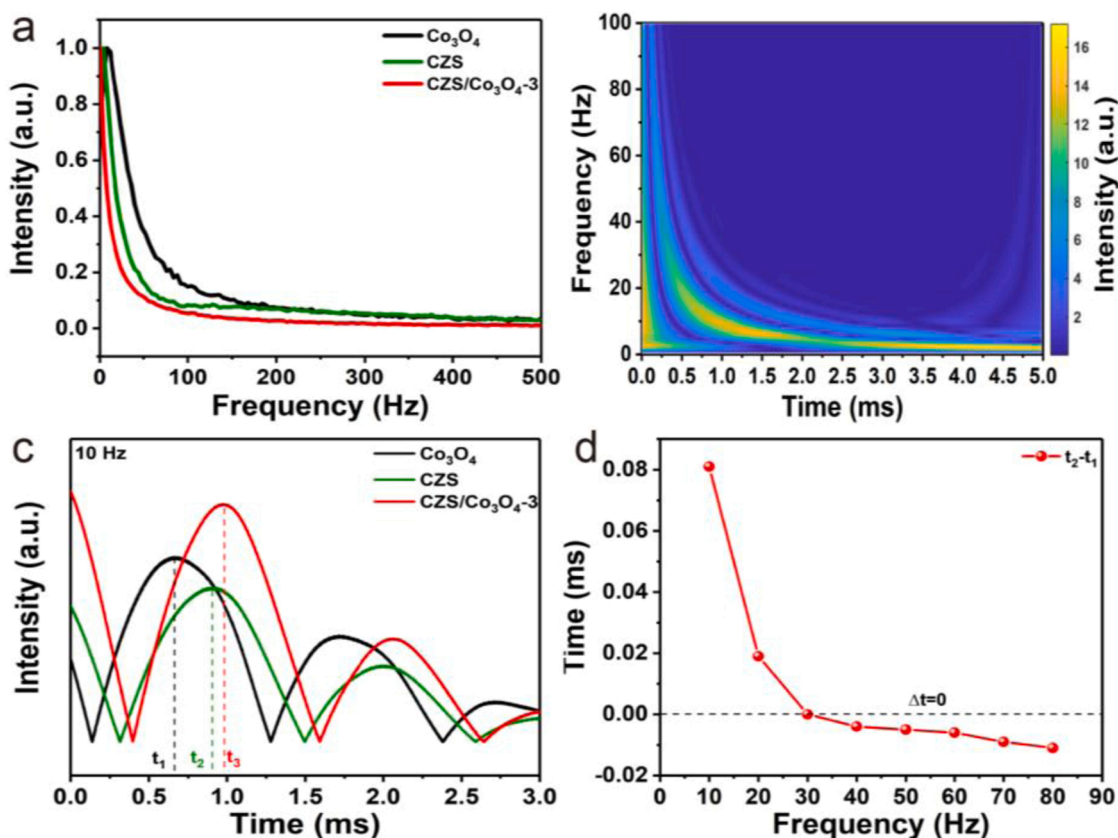
Fig. 7. (a) FFT spectra of Co_3O_4, CZS and CZS/Co_3O_4-3, (b) 2D CWT spectrum of CZS/Co_3O_4-3, (c) Intensity-Time curves (f = 10 Hz) of Co_3O_4, CZS and CZS/Co_3O_4-3 (t_1, t_2, and t_3 are the peak occurrence time of Co_3O_4, CZS and CZS/Co_3O_4-3, respectively), and (d) Peak delay time (Δt) at different frequencies (f = 10–80 Hz) for CZS and CZS/Co_3O_4-3.
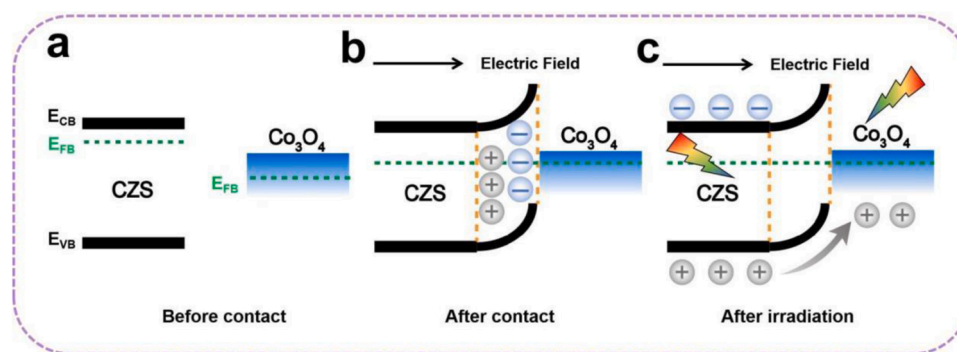
Fig. 8. (a) The band structure of CZS and Co_3O_4 before contact, (b) The electron transfer between CZS and Co_3O_4 when they are contacted in darkness, (c) photogenerated carrier transfer for CZS/Co_3O_4 photocatalyst under illumination.

such a case, the photo-generated electrons on the CB of CZS could reduce absorbed H_2O into H_2, while the photo-generated holes trapped by the Co_3O_4 to generate oxygen. Therefore, electrons and holes are directionally separated to the CZS and Co_3O_4, further inhibits the photo-corrosion of CZS caused by holes. Moreover, the one-dimensional nanorod structure with appropriate diameter ratio can effectively facilitate the directional transport and separation of photo-generated carries and shorten charge transfer distance to the surface. The holes are transferred to the surface-loaded Co_3O_4 over a shorter distance at surfaces, while the relatively long axis provides a channel for the migration of fast electrons, which significantly enhance the performance of the CZS photocatalyst.

4. Conclusions

In summary, we constructed CZS/Co_3O_4 composites consisting of well-dispersed Co_3O_4 nanoparticles anchoring on the CZS nanorods via a facile hydrothermal method. Combined with TPV and CWT analysis, the Co_3O_4 nanoparticles not only can attract and restrain more photogenerated holes to suppress photocorrosion, but also enhance the spatial charge isolation and prolong their lifetime. The optimized CZS/Co_3O_4 photocatalyst demonstrated remarkable photocatalytic performance with H_2 and O_2 production rate of 83.48 and 40.48 $\mu mol\ h^{-1}\ g^{-1}$ in pure water without any sacrificial agents. Meanwhile, satisfactory stability and photocatalytic activity were achieved in four-cycle reactions. This finding provides a new insight into fabricating effective and stable Cd-based photocatalyst for suppressing photocorrosion to drive pure water splitting under visible light and ambient conditions.

CRediT authorship contribution statement

Kai Yu: Conceptualization, Formal analysis, Writing – original draft. **Tianyang Zhang:** Investigation. **Yingming Wang:** Investigation. **Jie Wu:** Investigation. **Hui Huang:** Supervision. **Kui Yin:** Investigation. **Fan Liao:** Writing – review & editing, Supervision. **Yang Liu:** Supervision, Funding acquisition. **Zhenhui Kang:** Supervision, Funding acquisition.

Declaration of Competing Interest

The authors declare that they have no known competing financial interests or personal relationships that could have appeared to influence the work reported in this paper.

Data Availability

Data will be made available on request.

Acknowledgements

Associated content

None.

Supporting Information

Experimental section and additional figures.

Appendix A. Supporting information

Supplementary data associated with this article can be found in the online version at doi:10.1016/j.apcatb.2022.122228.

References

[1] J. Liu, Y. Liu, N. Liu, Y. Han, X. Zhang, H. Huang, Y. Lifshitz, S.T. Lee, J. Zhong, Z. Kang, Water splitting. Metal-free efficient photocatalyst for stable visible water splitting via a two-electron pathway, Science 347 (2015) 970–974, https://doi.org/10.1126/science.aaa3145.

[2] K. Takanabe, Photocatalytic water splitting: quantitative approaches toward photocatalyst by design, ACS Catal. 7 (2017) 8006–8022, https://doi.org/10.1021/acscatal.7b02662.

[3] L. Shang, B. Tong, H. Yu, G.I.N. Waterhouse, C. Zhou, Y. Zhao, M. Tahir, L.-Z. Wu, C.-H. Tung, T. Zhang, CdS nanoparticle-decorated Cd nanosheets for efficient visible light-driven photocatalytic hydrogen evolution, Adv. Energy Mater. 6 (2016) 1501241, https://doi.org/10.1002/aenm.201501241.

[4] B.-J. Ng, L.K. Putri, X.Y. Kong, P. Pasbakhsh, S.-P. Chai, Overall pure water splitting using one-dimensional P-doped twinned $Zn_{0.5}Cd_{0.5}S_{1-x}$ nanorods via synergetic combination of long-range ordered homojunctions and interstitial S vacancies with prolonged carrier lifetime, Appl. Catal. B Environ. 262 (2020), 118309, https://doi.org/10.1016/j.apcatb.2019.118309.

[5] X. Ning, G. Lu, Photocorrosion inhibition of CdS-based catalysts for photocatalytic overall water splitting, Nanoscale 12 (2020) 1213–1223, https://doi.org/10.1039/c9nr09183a.

[6] K. Yu, H.B. Huang, X.Y. Zeng, J.Y. Xu, X.T. Yu, H.X. Liu, H.L. Cao, J. Lu, R. Cao, CdZnS nanorods with rich sulphur vacancies for highly efficient photocatalytic hydrogen production, Chem. Commun. 56 (2020) 7765–7768, https://doi.org/10.1039/d0cc00522c.

[7] R. Shi, H.F. Ye, F. Liang, Z. Wang, K. Li, Y. Weng, Z. Lin, W.F. Fu, C.M. Che, Y. Chen, Interstitial P-doped CdS with long-lived photogenerated electrons for photocatalytic water splitting without sacrificial agents, Adv. Mater. 30 (2018) 1705941, https://doi.org/10.1002/adma.201705941.

[8] Z. Qiu, B. Wang, X. Zhou, S. Yang, Q. Gao, X. Cai, S. Zhang, Y. Fang, CdS@Mg(OH)$_2$ core/shell composite photocatalyst for efficient visible-light photocatalytic overall water splitting, Int. J. Hydrog. Energy 47 (2022) 8729–8738, https://doi.org/10.1016/j.ijhydene.2021.12.216.

[9] Y. Liu, X. Xu, S. Zheng, S. Lv, H. Li, Z. Si, X. Wu, R. Ran, D. Weng, F. Kang, Ni single atoms anchored on nitrogen-doped graphene as H$_2$-Evolution cocatalyst of SrTiO$_3$(Al)/CoO for photocatalytic overall water splitting, Carbon 183 (2021) 763–773, https://doi.org/10.1016/j.carbon.2021.07.064.

[10] B. Ma, Y. Dang, D. Li, X. Wang, K. Lin, W. Wang, X. Zhou, Y. Chen, T. Xie, X. Zhang, H. Han, A Yin-Yang hybrid co-catalyst (CoO$_x$-Mo$_2$N) for photocatalytic overall water splitting, Appl. Catal. B Environ. 298 (2021), 120491, https://doi.org/10.1016/j.apcatb.2021.120491.

[11] J. Zhang, T. Bai, H. Huang, M.H. Yu, X. Fan, Z. Chang, X.H. Bu, Metal-organic-framework-based photocatalysts optimized by spatially separated cocatalysts for overall water splitting, Adv. Mater. 32 (2020), e2004747, https://doi.org/10.1002/adma.202004747.

[12] X. Xie, N. Zhang, Z.-R. Tang, M. Anpo, Y.-J. Xu, Ti$_3$C$_2$T$_x$ MXene as a Janus cocatalyst for concurrent promoted photoactivity and inhibited photocorrosion, Appl. Catal. B Environ. 237 (2018) 43–49, https://doi.org/10.1016/j.apcatb.2018.05.070.

[13] M. Wen, K. Mori, Y. Kuwahara, H. Yamashita, Plasmonic Au@Pd nanoparticles supported on a basic metal–organic framework: synergic boosting of H$_2$ production from formic acid, ACS Energy Lett. 2 (2016) 1–7, https://doi.org/10.1021/acsenergylett.6b00558.

[14] R. Asai, H. Nemoto, Q. Jia, K. Saito, A. Iwase, A. Kudo, A visible light responsive rhodium and antimony-codoped SrTiO$_3$ powdered photocatalyst loaded with an IrO$_2$ cocatalyst for solar water splitting, Chem. Commun. 50 (2014) 2543–2546, https://doi.org/10.1039/c3cc49279f.

[15] Z. Pan, S. Wang, P. Niu, M. Liu, X. Wang, Photocatalytic overall water splitting by spatially-separated Rh and RhO$_x$ cocatalysts on polymeric carbon nitride nanosheets, J. Catal. 379 (2019) 129–137, https://doi.org/10.1016/j.jcat.2019.09.016.

[16] M. Chen, X. Huang, C. Chen, W. Hou, Y. Xu, M-Dependent activity of MCo$_2$O$_4$ spinels for water splitting and H$_2$ production on Zn$_{0.5}$Cd$_{0.5}$S under visible light, Appl. Catal. B Environ. 298 (2021), 120469, https://doi.org/10.1016/j.apcatb.2021.120469.

[17] X. Ning, W. Zhen, Y. Wu, G. Lu, Inhibition of CdS photocorrosion by Al$_2$O$_3$ shell for highly stable photocatalytic overall water splitting under visible light irradiation, Appl. Catal. B Environ. 226 (2018) 373–383, https://doi.org/10.1016/j.apcatb.2017.12.067.

[18] Z. Zhao, J. Fan, X. Deng, J. Liu, One-step synthesis of phosphorus-doped g-C$_3$N$_4$/Co$_3$O$_4$ quantum dots from vitamin B12 with enhanced visible-light photocatalytic activity for metronidazole degradation, Chem. Eng. J. 360 (2019) 1517–1529, https://doi.org/10.1016/j.cej.2018.10.239.

[19] W. Wang, T. Li, S. Komarneni, X. Lu, B. Liu, Recent advances in Co-based co-catalysts for efficient photocatalytic hydrogen generation, J. Colloid Interface Sci. 608 (2022) 1553–1575, https://doi.org/10.1016/j.jcis.2021.10.051.

[20] Z. Liu, K. Zhang, B. Chang, Y. Shao, L. Zhang, Y. Wu, X. Hao, Construction of CdS@Ti$_3$C$_2$@CoO hierarchical tandem p-n heterojunction for boosting photocatalytic hydrogen production in pure water, Chem. Eng. J. 383 (2020) 123130, https://doi.org/10.1016/j.cej.2019.123130.

[21] J. Liu, J. Ke, Y. Li, B. Liu, L. Wang, H. Xiao, S. Wang, Co$_3$O$_4$ quantum dots/TiO$_2$ nanobelt hybrids for highly efficient photocatalytic overall water splitting, Appl. Catal. B Environ. 236 (2018) 396–403, https://doi.org/10.1016/j.apcatb.2018.05.042.

[22] W. Xue, X. Bai, J. Tian, X. Ma, X. Hu, J. Fan, E. Liu, Enhanced photocatalytic H$_2$ evolution on ultrathin Cd$_{0.5}$Zn$_{0.5}$S nanosheets without a hole scavenger: combined analysis of surface reaction kinetics and energy-level alignment, Chem. Eng. J. 428 (2022), 132608, https://doi.org/10.1016/j.cej.2021.132608.

[23] X. Tang, J. Li, J. Hao, Synthesis and characterization of spinel Co$_3$O$_4$ octahedra enclosed by the {111} facets, Mater. Res. Bull. 43 (2008) 2912–2918, https://doi.org/10.1016/j.materresbull.2007.12.009.

[24] H. Du, K. Liang, C.Z. Yuan, H.L. Guo, X. Zhou, Y.F. Jiang, A.W. Xu, Bare Cd$_{1−x}$Zn$_x$S ZB/WZ heterophase nanojunctions for visible light photocatalytic hydrogen production with high efficiency, ACS Appl. Mater. Interfaces 8 (2016) 24550–24558, https://doi.org/10.1021/acsami.6b06182.

[25] L. Liu, Z. Jiang, L. Fang, H. Xu, H. Zhang, X. Gu, Y. Wang, Probing the crystal plane effect of Co$_3$O$_4$ for enhanced electrocatalytic performance toward efficient overall water splitting, ACS Appl. Mater. Interfaces 9 (2017) 27736–27744, https://doi.org/10.1021/acsami.7b07793.

[26] H. Zhao, L. Guo, C. Xing, H. Liu, X. Li, A homojunction–heterojunction–homojunction scaffold boosts photocatalytic H$_2$ evolution over Cd$_{0.5}$Zn$_{0.5}$S/CoO hybrids, J. Mater. Chem. A 8 (2020) 1955–1965, https://doi.org/10.1039/c9ta11915a.

[27] X. Hao, D. Xiang, Z. Jin, Amorphous Co$_3$O$_4$ quantum dots hybridizing with 3D hexagonal CdS single crystals to construct a 0D/3D p-n heterojunction for a highly efficient photocatalytic H$_2$ evolution, Dalton Trans. 50 (2021) 10501–10514, https://doi.org/10.1039/d1dt01333e.

[28] C. Zhang, B. Liu, W. Li, X. Liu, K. Wang, Y. Deng, Z. Guo, Z. Lv, A well-designed honeycomb Co$_3$O$_4$@CdS photocatalyst derived from cobalt foam for high-efficiency visible-light H$_2$ evolution, J. Mater. Chem. A 9 (2021) 11665–11673, https://doi.org/10.1039/d0ta11433b.

[29] H. Shao, X. Zhao, Y. Wang, R. Mao, Y. Wang, M. Qiao, S. Zhao, Y. Zhu, Synergetic activation of peroxymonosulfate by Co$_3$O$_4$ modified g-C$_3$N$_4$ for enhanced degradation of diclofenac sodium under visible light irradiation, Appl. Catal. B Environ. 218 (2017) 810–818, https://doi.org/10.1016/j.apcatb.2017.07.016.

[30] N. Zhao, J. Peng, G. Liu, Y. Zhang, W. Lei, Z. Yin, J. Li, M. Zhai, PVP-capped CdS nanopopcorns with type-II homojunctions for highly efficient visible-light-driven organic pollutant degradation and hydrogen evolution, J. Mater. Chem. A 6 (2018) 18458–18468, https://doi.org/10.1039/c8ta03414a.

[31] L.L.K. Gelderman, S.W. Donne, Flat-band potential of a semiconductor: using the Mott–Schottky EQuation, J. Chem. Educ. 84 (2007) 685, https://doi.org/10.1021/ed084p685.

[32] L.K. Putri, B.-J. Ng, W.-J. Ong, H.W. Lee, W.S. Chang, S.-P. Chai, Engineering nanoscale p–n junction via the synergetic dual-doping of p-type boron-doped graphene hybridized with n-type oxygen-doped carbon nitride for enhanced photocatalytic hydrogen evolution, J. Mater. Chem. A 6 (2018) 3181–3194, https://doi.org/10.1039/c7ta09723a.

[33] H.-B. Huang, Z.-B. Fang, K. Yu, J. Lü, R. Cao, Visible-light-driven photocatalytic H$_2$ evolution over CdZnS nanocrystal solid solutions: interplay of twin structures, sulfur vacancies and sacrificial agents, J. Mater. Chem. A 8 (2020) 3882–3891, https://doi.org/10.1039/c9ta13836f.

[34] T. Jia, J. Wu, Y. Xiao, Q. Liu, Q. Wu, Y. Qi, X. Qi, Self-grown oxygen vacancies-rich CeO$_2$/BiOBr Z-scheme heterojunction decorated with rGO as charge transfer channel for enhanced photocatalytic oxidation of elemental mercury, J. Colloid Interface Sci. 587 (2021) 402–416, https://doi.org/10.1016/j.jcis.2020.12.005.

[35] Y. Liu, Y. Zhao, Q. Wu, X. Wang, H. Nie, Y. Zhou, H. Huang, M. Shao, Y. Liu, Z. Kang, Charge storage of carbon dot enhances photo-production of H$_2$ and H$_2$O$_2$ over Ni$_2$P/carbon dot catalyst under normal pressure, Chem. Eng. J. 409 (2021), 128184, https://doi.org/10.1016/j.cej.2020.128184.

[36] R. Konta, T. Ishii, H. Kato, A. Kudo, Photocatalytic activities of noble metal ion doped SrTiO$_3$ under visible light irradiation, J. Phys. Chem. B 108 (2004) 8992–8995, https://doi.org/10.1021/jp049556p.

[37] T. He, J. Wu, Y. Li, K. Wei, Y. Liu, H. Huang, Y. Liu, Z. Kang, A step-by-step design for dual channel metal-free photocatalysts towards high yield H$_2$O$_2$ photo-production from air and water, Chem. Eng. J. 451 (2023), 138551, https://doi.org/10.1016/j.cej.2022.138551.

[38] Z. Wu, X. Wang, Y. Li, H. Zhao, J. Wang, H. Huang, Y. Liu, Z. Kang, Converting water impurity in organic solvent into hydrogen and hydrogen peroxide by organic semiconductor photocatalyst, Appl. Catal. B Environ. 305 (2022), 121047, https://doi.org/10.1016/j.apcatb.2021.121047.

[39] X. Gu, C. Chen, Y. Li, X. Wang, H. Huang, Y. Liu, B. Dong, M. Shao, Z. Kang, Polyaniline/carbon dots composite as a highly efficient metal-free dual-functional photoassisted electrocatalyst for overall water splitting, ACS Appl. Mater. Interfaces 13 (2021) 24814–24823, https://doi.org/10.1021/acsami.1c04386.

[40] Y. Liu, X. Wang, Y. Zhao, Q. Wu, H. Nie, H. Si, H. Huang, Y. Liu, M. Shao, Z. Kang, Highly efficient metal-free catalyst from cellulose for hydrogen peroxide photoproduction instructed by machine learning and transient photovoltage technology, Nano Res. 15 (2022) 4000–4007, https://doi.org/10.1007/s12274-022-4111-2.

[41] F. Liao, Y. Shi, Q. Dang, H. Yang, H. Huang, Z. Kang, M. Shao, Carbon dots dominated photoelectric surface in titanium dioxide nanotube/nitrogen-doped carbon dot/gold nanocomposites for improved photoelectrochemical water splitting, J. Colloid Interface Sci. 606 (2022) 1274–1283, https://doi.org/10.1016/j.jcis.2021.08.131.

[42] F. Li, Y. Liu, Q. Chen, X. Gu, W. Dong, D. Zhang, H. Huang, B. Mao, Z. Kang, W. Shi, Transient photovoltage study of the kinetics and synergy of electron/hole co-extraction in MoS$_2$/Ag-In-Zn-S/carbon dot photocatalysts for promoted hydrogen production, Chem. Eng. J. 439 (2022), 135759, https://doi.org/10.1016/j.cej.2022.135759.

[43] H. Nie, Y. Liu, Y. Li, K. Wei, Z. Wu, H. Shi, H. Huang, Y. Liu, M. Shao, Z. Kang, In-situ transient photovoltage study on interface electron transfer regulation of carbon dots/NiCo$_2$O$_4$ photocatalyst for the enhanced overall water splitting activity, Nano Res. 15 (2021) 1786–1795, https://doi.org/10.1007/s12274-021-3723-2.

[44] Y. Liu, J. Wang, J. Wu, Y. Zhao, H. Huang, Y. Liu, Z. Kang, Critical roles of H$_2$O and O$_2$ in H$_2$O$_2$ photoproduction over biomass derived metal-free catalyst, Appl. Catal. B Environ. 319 (2022), 121944, https://doi.org/10.1016/j.apcatb.2022.121944.

[45] P. Xia, S. Cao, B. Zhu, M. Liu, M. Shi, J. Yu, Y. Zhang, Designing a 0D/2D S-scheme heterojunction over polymeric carbon nitride for visible-light photocatalytic inactivation of bacteria, Angew. Chem. Int. Ed. 59 (2020) 5218–5225, https://doi.org/10.1002/anie.201916012.

[46] C. Peng, P. Wei, X. Li, Y. Liu, Y. Cao, H. Wang, H. Yu, F. Peng, L. Zhang, B. Zhang, K. Lv, High efficiency photocatalytic hydrogen production over ternary Cu/TiO$_2$@Ti$_3$C$_2$T$_x$ enabled by low-work-function 2D titanium carbide, Nano Energy 53 (2018) 97–107, https://doi.org/10.1016/j.nanoen.2018.08.040.